

Active Galactic Nuclei in a Mid-Infrared Selected Galaxy Sample at $z > 0.13$: [Ne V] λ 3426 Line Emission as a Benchmark

ZI-JIAN LI,^{1,2} Y. SOPHIA DAI,¹ JIA-SHENG HUANG,^{1,3} STIJN WUYTS,⁴ AND TIAN-WEN CAO⁵

¹*Chinese Academy of Sciences South America Center for Astronomy (CASSACA),
National Astronomical Observatories of China (NAOC),
CAS, 20A Datun Road, Beijing 100012, China*

²*School of Astronomy and Space Sciences, University of Chinese Academy of Sciences, Beijing 100049, China*

³*Harvard-Smithsonian Center for Astrophysics, 60 Garden Street, Cambridge, MA 02138, USA*

⁴*Department of Physics, University of Bath, Claverton Down, Bath, BA2 7AY, UK*

⁵*Department of Astronomy, Xiamen University, 422 Siming South Road, Xiamen 361005, China*

(Accepted by ApJ January 4, 2024)

ABSTRACT

We present a $24\mu\text{m}$ -selected spectroscopic sample $z > 0.13$ (median $\langle z \rangle = 0.41$) in the Lockman Hole field, consisting of 4035 spectra. Our aim is to identify AGNs and determine their fraction in this mid-infrared selected sample. In this work, we use the [Ne V] λ 3426 emission line to spectroscopically identify AGNs. Combined with broad-line Type I AGNs selected in our previous study, our sample consists of 887 ($\sim 22\%$) spectroscopically confirmed AGNs. We perform a stacking analysis on the remaining spectra, and find that in various MIR-wedge-selected AGN candidates, the stacked spectra still show significant [Ne V] λ 3426 emission. In contrast, no clear [Ne V] λ 3426 signal is detected in non-AGN candidates falling outside the wedges. Assuming a range of AGN mid-IR SED slope of $-0.3 < \alpha < 0.7$, and an average star-forming relation derived from 65 star-forming templates, we develop a robust method to separate the AGN and star-forming contributions to the mid-IR SEDs using the rest-frame $L_{12}/L_{1.6}$ vs $L_{4.5}/L_{1.6}$ diagram. We separate the objects into bins of L_{12} , and find that AGN fraction increases with increasing L_{12} . We also find that the stacked [Ne V] λ 3426 strength scales with L_{12} . The pure AGN luminosity at $12\mu\text{m}$ exhibits a positive correlation with the star formation rates, indicating possible co-evolution and common gas supply between the AGN and their host galaxies. Varying population properties across the redshift range explored contribute to the observed correlation.

Keywords: Active galactic nuclei — Star formation

1. INTRODUCTION

Active galactic nuclei (AGN) play a crucial role in galaxy evolution, as demonstrated by previous studies highlighting strong correlations between central black hole mass and host properties (Ferrarese & Merritt 2000; Gebhardt et al. 2000; Tremaine et al. 2002; Marconi & Hunt 2003; Häring & Rix 2004; Gültekin et al. 2009; McConnell & Ma 2013). It has been proposed that when a host experiences bulge growth, e.g. through merging, a central black hole will accrete rapidly (Hopkins et al.

2006). Additionally, infrared observations have shown that AGNs are typically present in galaxies with intense star formation (Farrah et al. 2003; Rosario et al. 2012; Santini et al. 2012; Cresci et al. 2015; Dai et al. 2018; Shin et al. 2019; Xie et al. 2021). However, it is also believed that AGNs play a role in suppressing star formation (Croton et al. 2006; Ciotti et al. 2010; Fabian 2012; Page et al. 2012; Jin et al. 2021). Without this suppression, models predict more massive galaxies than observed (Bower et al. 2006). Thus, understand the relationship between AGN and star formation activities is critical to understanding the process of galaxy evolution.

Various methods for identifying AGNs in galaxies have been employed (Padovani et al. 2017; Hickox & Alexan-

der 2018; Lyu et al. 2022). The most common approach has been to use spectral signatures. AGNs can be classified into two types based on their spectra: Type I AGNs feature broad lines, whereas Type II AGNs have only narrow lines as their Broad Line Region (BLR) emission is presumed to be blocked by dust (Vanden Berk et al. 2001; Hao et al. 2005). Type II AGNs are more prevalent in galaxy samples (Hickox & Alexander 2018). Baldwin et al. (1981, hereafter BPT) proposed narrow line ratio diagnostics to separate AGNs from star forming galaxies (e.g., $[\text{O III}]/\text{H}\beta$ versus $[\text{N II}]/\text{H}\alpha$). However, this BPT method (Kauffmann et al. 2003; Kewley et al. 2006) is only applicable for optical spectroscopic galaxy samples at $z < 0.4$, when $\text{H}\alpha$ remains in the optical band. Alternative methods using either rest-frame color or stellar mass, together with the $[\text{O III}]/\text{H}\beta$ line ratio, have been developed to identify AGNs in galaxies at $z > 0.4$ (Yan et al. 2011; Juneau et al. 2011, 2014), likewise exploiting high excitation lines as a marker of nuclear activity. Zakamska et al. (2003); Reyes et al. (2008) constructed Type II quasar samples on the basis of their $[\text{O III}]$ luminosity, but this method is only effective for quasars with extremely strong $[\text{O III}]$ lines. Among more moderate luminosity systems, star formation can also excite $[\text{O III}]$ emission, thus compromising the approach (Suzuki et al. 2016). On the other hand, $[\text{Ne V}]\lambda 3426$ is a line that only appears in AGN spectra due to its high ionization potential, making it an attractive diagnostic tool for nuclear activity (Mignoli et al. 2013; Cleri et al. 2022). Its shorter wavelength compared to $[\text{O III}]\lambda 5007$ implies it can be traced out to higher redshifts with optical spectrographs, at the expense of a greater sensitivity to dust obscuration (Gilli et al. 2010; Vignali et al. 2014).

In the absence of spectroscopic diagnostics, AGNs can also be identified on the basis of spectral energy distribution (SED) features. In most infrared-selected galaxy samples, spectroscopic observations are expensive, and usually not feasible for every galaxy. To achieve this, several mid-infrared (MIR) color selections, also referred to as AGN wedges, were proposed (Lacy et al. 2004; Stern et al. 2005; Donley et al. 2012; Assef et al. 2013). Though using different MIR colors, their selections in essence aim to isolate sources whose SEDs are dominated by the characteristic power-law emission of an AGN in the rest-frame MIR band (Donley et al. 2012). These selections are usually applied to bright galaxy samples. Contamination by high-redshift galaxies becomes more severe if extended to fainter samples (Assef et al. 2010). Despite their popularity, spectroscopic or X-ray observations remain the ultimate source of confirmation for AGNs. Some spectroscopic observations on

infrared-selected AGN candidates confirmed that about 80% of their targets were AGNs, mainly of a dust obscured nature (Lacy et al. 2007; Hainline et al. 2014; Lacy et al. 2013). Major observational campaigns with X-ray telescopes have also mapped the infrared survey fields (Nandra et al. 2005; Wilkes et al. 2009; Nandra et al. 2015; Civano et al. 2016; Luo et al. 2017). Nandra et al. (2015) found that about 90% of their X-ray sources have MIR counterparts. Donley et al. (2012) further found that X-ray selected AGNs that predominantly reside in a small region within the broader Lacy AGN color wedge (Lacy et al. 2004). Though X-rays represent a powerful technique to detect AGNs, some AGNs suffer from intrinsic extinction, and consequently can be absent from even the deepest X-ray observations (Alonso-Herrero et al. 2006; Donley et al. 2007).

In this paper, we present a spectroscopic study of a MIPS $24\mu\text{m}$ bright sample: these targets are selected from SWIRE survey (Lonsdale et al. 2003) with $F_{24} > 400\mu\text{Jy}$ in the Lockman Hole field. We aim to provide a census of AGN in this infrared sample, which spans the redshift range of $z = 0 - 6$, with $\sim 90\%$ of objects located below $z = 1.4$. $[\text{Ne V}]\lambda 3426$ emission serves as the primary AGN diagnostic in this study, where relevant augmented by BLR detections. We also adopt the MIR AGN color selection designed by Lacy et al. (2004) and Donley et al. (2012) for the dusty objects in our sample, and stack their spectra to search for the presence of $[\text{Ne V}]\lambda 3426$ as AGN confirmation. We develop a method to isolate the AGN contribution to the SEDs of all objects in our spectroscopic sample, and study the relation between AGN and star formation activities.

The paper is organized as follows. In Section 2, we present the $24\mu\text{m}$ selected spectroscopic sample and associated multiwavelength data. The AGN selection methods are outlined in Section 3. Section 4 presents the composite spectra of the whole spectroscopic sample and the confirmation of AGN activity via stacking. In Section 5, we present the SED decomposition into emission from AGN and star formation. Section 6 next presents the derived properties for all objects in our sample and discusses the relation between AGNs and their hosts. We summarize our conclusions in Section 7. Throughout the paper, we adopt a standard ΛCDM cosmology with $H_0 = 70 \text{ km s}^{-1} \text{ Mpc}^{-1}$, $\Omega_M = 0.3$ and $\Omega_\lambda = 0.7$. The initial mass function (IMF) used in this paper is from Kroupa (2001).

2. SAMPLE AND DATA

2.1. Spectroscopic sample

Dai et al. (2014) conducted a redshift survey on a MIPS $24\mu\text{m}$ selected sample. The observations were

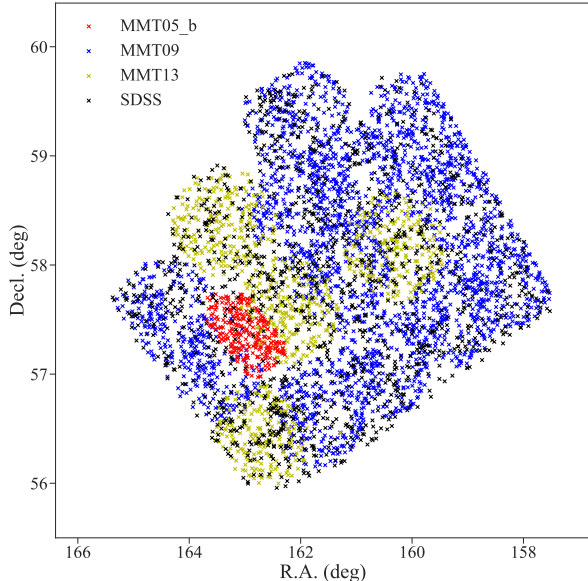


Figure 1. Spatial distribution of spectroscopic coverage. The red, blue, yellow and black crosses are spectra observed in the MMT05_b, MMT09 and MMT13 runs, and as part of the SDSS survey, respectively. The original MMT05 survey adopted a deeper $24\mu\text{m}$ limit: $F_{24} > 60\mu\text{Jy}$. To ensure uniformity, we here keep the flux limit as $F_{24} > 400\mu\text{Jy}$ and label this subset with subscript b.

done with Hectospec on MMT, an optical spectrograph (3850\AA - 8300\AA) with 300 fibers deployed over a 1 deg^2 field of view. The targets were chosen from the SWIRE survey (Lonsdale et al. 2003) with $F_{24} > 400\mu\text{Jy}$ and $r < 22.5\text{ mag}$.¹ There are 23,402 sources with $F_{24} > 400\mu\text{Jy}$ within the 22 deg^2 area of the Lockman Hole field. Of these, 12,245 ($\sim 52\%$) of sources are also brighter than $r = 22.5$. In total, we configured 3,757 targets for observation, avoiding objects with existing SDSS redshifts in each Hectospec configuration. Dai et al. (2014) presented the observing strategy for this redshift survey, in which they assigned each spectrum a redshift quality flag ranging from 1 to 4. Robust redshifts were extracted for 3463 of the spectra (quality flags 3 and 4). We further augmented the dataset with 1,317 spectra from SDSS DR17. Thus the total sample consists of 4780 spectra, a total of 4035 out of 4780 spectra have $z > 0.13$. Figure 1 shows the layout of our survey in the Lockman-Hole field. Example spectra for different spectral types are illustrates in Figure 2.

We present the success rate of obtaining spectroscopic redshifts for the $24\mu\text{m}$ selected sources in Figure 3. The identification rate remains approximately constant (and

high) with varying $24\mu\text{m}$ flux at r -band magnitudes brighter than 17.7. The median value is 98%. Below this limit, the success rate increases with increasing $24\mu\text{m}$ flux, from around 40% at the faint end to about 70% when the $24\mu\text{m}$ magnitude is brighter than 16.3 ($\sim 1000\mu\text{Jy}$). The median redshift success rate among all targets with $17.7 < r < 22.5$ is 54%.

2.2. Multiwavelength data

We collected multiwavelength photometry for our spectroscopic sample from the rich ancillary data in the Lockman Hole field. We cross-matched our sources with the Sloan Digital Sky Survey (SDSS) Data Release 17 (DR17) database, which provides photometric measurements (cModelMag) in the u , g , r , i , and z bands (Abdurro’uf et al. 2022). For the near-infrared (NIR), we derived J and K magnitudes within a $2''$ aperture using images from the UKIRT Infrared Deep Sky Survey (UKIDSS) DXS DR11PLUS (Lawrence et al. 2007). The magnitudes were then aperture-corrected with a constant percentage appropriate for point sources. In the MIR, we utilized aperture photometry provided by the SWIRE survey (Lonsdale et al. 2003), which covers a wavelength range of $3.6\text{--}24\mu\text{m}$. Finally, we obtained far-infrared (FIR) flux measurements from the Herschel Multi-tiered Extragalactic Survey (HerMES) in five bands spanning $100\text{--}500\mu\text{m}$ (Roseboom et al. 2010). The Herschel photometry was extracted using the XID algorithm using the positions of $24\mu\text{m}$ sources as priors (Oliver et al. 2012).

We list the numbers and fractions of 3σ detections in each band in Table 1.

3. AGN CONFIRMATION

Both AGN and star formation activities can contribute to the observed MIR emission. To study the connection between AGNs and their hosts, it is crucial to firstly identify AGNs and estimate their contribution in a MIR-selected sample. While the BPT diagram is a commonly used tool for identifying AGNs spectroscopically, its effectiveness is limited to low-redshift objects (Juneau et al. 2011), with only about 30% of our spectra falling within a redshift range where BPT diagnostics are applicable. On the other hand, the $[\text{Ne V}]\lambda 3426$ line is considered a reliable AGN indicator (Abel & Satyapal 2008). Approximately 75% of our spectra cover the rest-frame $[\text{Ne V}]\lambda 3426$ line region (i.e., those with a redshift between 0.13 and 1.40). Here we note that $[\text{Ne V}]$ emission has doublet signals (peak at 3346 and 3426\AA) in the optical regime. The 3346 line flux is usually one third of that of 3426 line (e.g., Vanden Berk et al. 2001), thus

¹ The r is the SDSS r -band model magnitude.

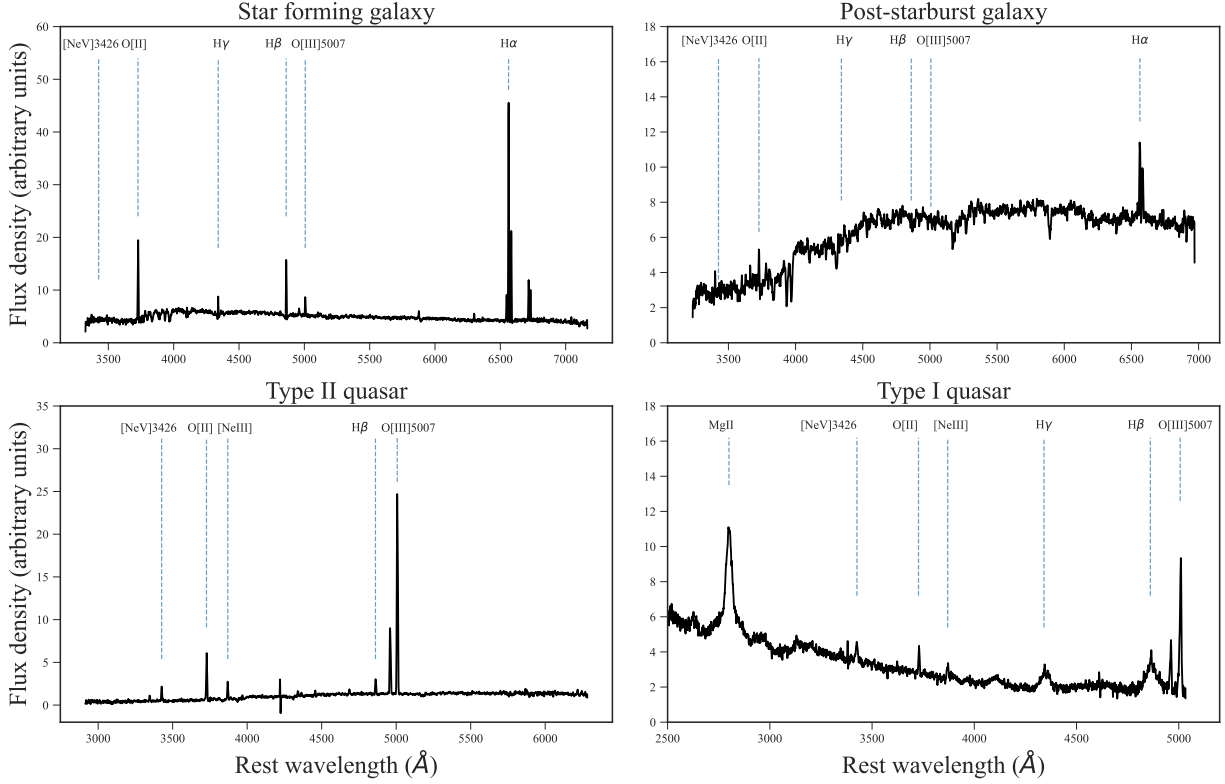


Figure 2. Example spectra in rest-frame from our sample. *Upper left panel:* Example of a star-forming galaxy. *Upper right panel:* Example of a post-starburst galaxy. *Lower left panel:* Example of a Type II quasar. *Lower right panel:* Example of a Type I quasar.

Table 1. Multiwavelength data coverage.

Band	$N_{3\sigma}$	$P_{3\sigma}$
SDSS DR17		
u	3402	71%
g	4589	96%
r	4751	99%
i	4766	99%
z	4446	93%
UKIDSS DXS		
J	3587	75%
K	3594	75%
SWIRE		
3.6 μm	4396	92%
4.5 μm	4396	92%
5.8 μm	3940	82%
8.0 μm	4049	85%
24 μm	4780	100%
HerMES		
100 μm	1775	37%
160 μm	1496	31%
250 μm	2476	52%
350 μm	1131	24%
500 μm	347	7%

NOTE— $N_{3\sigma}$ and $P_{3\sigma}$ are the numbers and percentages of 3σ detections in each band, respectively.

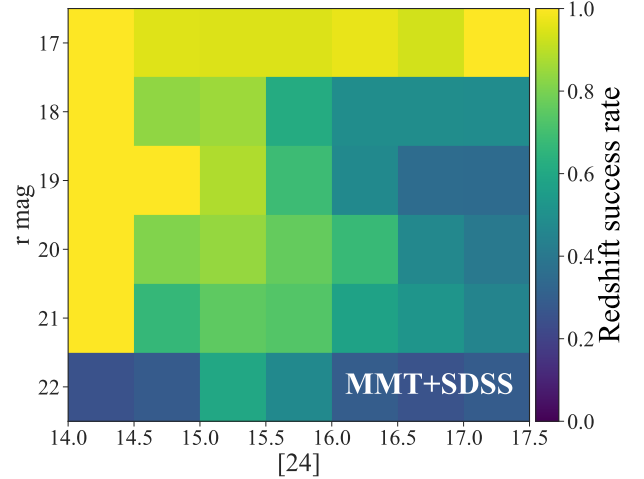


Figure 3. Spectroscopic identification rate of our sample in the Lockman-Hole field. Redshifts used here are mainly from D14, with redshifts for the brightest objects in this field being supplemented from SDSS. Each spectrum in Dai et al. (2014) was assigned a redshift quality flag from 4 to 1. Spectra with quality flags 3 or 4 are considered to yield reliable redshifts, which are used for the statistics in this diagram.

throughout the paper we use the 3426 signal to confirm AGNs. The 3346 line is marked in the figures for display

purpose but not used for analysis in this paper. For the 487 spectra ($\sim 10\%$ of the whole sample) with $z > 1.40$, we find that most of them ($\sim 92\%$) are broad line AGNs. We refer the reader to Dai et al. (2014) for more details on this broad-line AGN sample and selection methods. In the following section, we start by identifying AGNs with individual [Ne V] $\lambda 3426$ detections in the redshift range $0.13 < z < 1.40$.

3.1. [Ne V] $\lambda 3426$ selection

To identify [Ne V] $\lambda 3426$ emission, we calculate the equivalent width (EW) and signal-to-noise ratio (SNR) of the [Ne V] $\lambda 3426$ region for each spectrum. We firstly define the line region as $(\lambda_0 \pm 13)\text{\AA}$. Here, λ_0 represents the line center defined as

$$\lambda_0 = \frac{\sum n_0 \lambda I_\lambda}{\sum n_0 I_\lambda}, \quad (1)$$

where n_0 is the number of pixels in the rest-frame wavelength range $3413\text{-}3439\text{\AA}$. The 13\AA width is motivated by summing the typical [Ne V] $\lambda 3426$ line width ($3\sigma \sim 11\text{\AA}$) and velocity shift of about 2\AA relative to [O II] line center (Vanden Berk et al. 2001).

The SNRs are also calculated in the same line region using the following expression:

$$SNR = \frac{\sum_n I_\lambda - I_c}{\sqrt{n}\sigma_c}, \quad (2)$$

where n is the number of pixels in the line region, I_c is the continuum intensity, I_λ is the spectral intensity and σ_c is the standard deviation of the continuum-subtracted intensity in the continuum region. We initially select 94 objects based on $SNR > 3$. To ensure the fidelity of our sample, we conduct visual inspections to remove any fake detections caused by incorrect telluric line subtraction. Finally, we identify a total of 88 [Ne V] $\lambda 3426$ -selected AGNs, with 43 of them being narrow-line Type II AGNs.

3.2. The equivalent width bias

Previous studies have suggested that the equivalent width (EW) of [Ne V] $\lambda 3426$ could be related to the degree of nuclear extinction (Yan et al. 2021). In Type II AGNs, the torus obscures the continuum emission from the central region along the line of sight, leading to an increase of the EW of the emission line from the outer narrow-line region (NLR) (Levenson et al. 2002).

We plot the Type I fraction among our [Ne V] $\lambda 3426$ selected sample as a function of EW in Figure 4. The fraction is defined as the ratio between the number of Type I AGN and the total number of AGN. We find that the fraction decreases from 90% to 10% when the EW

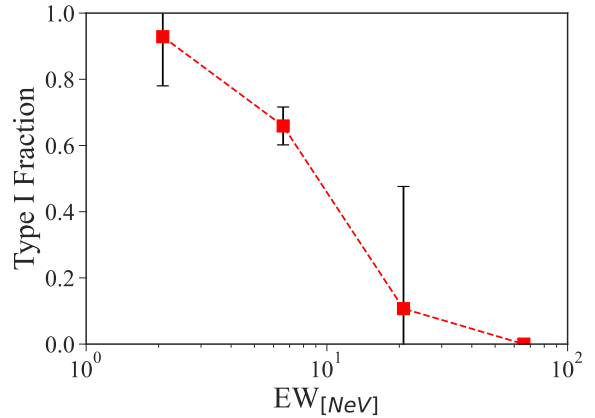


Figure 4. Type I AGN fraction versus the equivalent width (EW) of [Ne V] $\lambda 3426$ for our [Ne V] $\lambda 3426$ selected AGN sample. The error bars show the Poisson uncertainty.

increases from $\sim 2\text{\AA}$ to 20\AA . This result quantitatively illustrates the EW bias.

3.3. The spectroscopically confirmed AGN sample

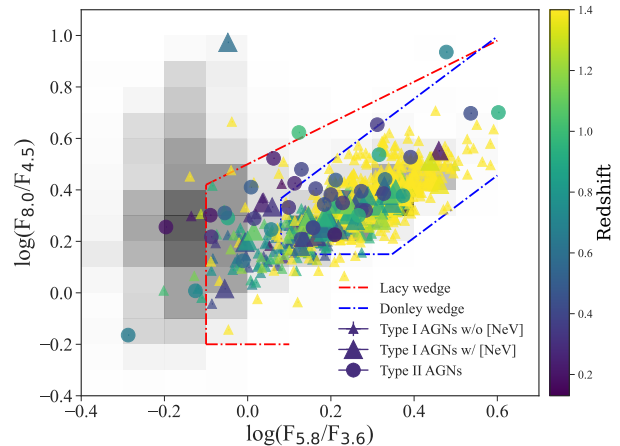


Figure 5. Observed-frame color-color diagram of our spectroscopically confirmed AGNs. The greyscales denote the $24\text{ }\mu\text{m}$ bright spectroscopic sample with secure redshifts. Triangle symbols mark the 844 Type I AGNs (A total of 45 of them have [Ne V] $\lambda 3426$ detections and these 45 objects are marked as triangles with larger size.) and circles mark the 43 Type II AGNs. Colors indicate their redshifts.

The red and blue dash-dotted lines indicate the Lacy and Donley wedges, respectively.

The sample of broad-line AGN among our parent dataset was compiled by Dai et al. (2014). The combination of the [Ne V] $\lambda 3426$ and broad-line selections now provides a more complete picture of the AGN population. This results in a total of 887 sources in our spectroscopically confirmed AGN sample. A total of 43 objects are [Ne V] $\lambda 3426$ selected Type II AGNs and the

remaining 844 objects are Type I from Dai et al. (2014). Among these Type I AGNs, there are 45 objects that also have [Ne V] λ 3426 detections.

Compared with MIR color selections of AGN, our optical spectroscopy confirms that 53% and 84% of AGN candidates¹ selected by Lacy’s and Donley’s criteria, respectively, are true AGNs. As shown in Figure 5, the Donley wedge is more successful in selecting strong AGNs at high redshifts.

4. OPTICAL SPECTRA OF MIR-SELECTED SAMPLE

4.1. Composite spectra

In this section, we present the composite spectra of objects in our spectroscopic sample and search for potential AGN signals across the MIR color space. To this end, we divide our sample into 10 subsets based on their position in the MIR color-color diagram (see Figure 6). Each bin covers 0.2 dex in $\log(F_{5.8}/F_{3.6})$ and 0.3 dex in $\log(F_{8.0}/F_{4.5})$. Where relevant, we label each bin by the coordinates of the lower-left corner (xmin, ymin). To build the composite spectrum of each bin, we firstly shift all spectra to the rest frame and then normalize them to a common continuum level. Given the spread in redshifts within and between bins, the continuum level used for normalization is determined as the median flux in the rest-frame 2100-2200 \AA range for the (0.3,0.3) bin, the rest-frame 3100-3200 \AA range for the (0.1,0.2) bin, and the rest-frame 4200-4300 \AA range for the remaining bins. A common wavelength grid from 2500 to 5200 \AA was built, with wavelength steps of 6 \AA . In each color bin, we then construct the composite spectra by taking the median value of all the normalized data points included. The results are shown in the left panel of Figure 6. We can observe clear broad Mg II line features in the two bins within the Donley wedge (i.e., the (0.1,0.2) and (0.3,0.3) bins). They also show narrow $H\beta$ and strong [O III] lines. This is because coverage of those lines requires relatively low redshifts, where in our sample the AGN family is in numbers dominated by Type II AGNs. The spectrum in the (0.1,0.2) bin shows weaker and narrower Mg II line compared to the spectrum in the (0.3,0.3) bin. Additionally, it displays a flatter blue continuum (Zakamska et al. 2003). Zhang & Hao (2018) have developed the kinematic excitation (KEx) diagram, which uses [O III] λ 5007/ $H\beta$ line ratio and velocity dispersion of [O III] λ 5007 line, to classify the ionization source. We also label the KEx classification for each

composite spectrum in the inset panel. We find that Donley objects are more like AGNs while the Lacy objects tend to be like composite galaxies. The classification is also found to be consistent with the SNR of stacked [Ne V] λ 3426. However, the [Ne V] λ 3426 stacking in the (-0.1,-0.2) bin shows an insufficient signal-to-noise ratio, which could be attributed to the smaller number of spectra available in that bin. Details on the [Ne V] λ 3426 stacking procedure and further discussions are provided in Section 4.2.

4.2. AGN signals in color selected candidates

In this section we stack spectra to search for [Ne V] λ 3426 signals in the redshift range $0.13 < z < 1.40$ for all of our sources. Firstly, all of the spectra are shifted to rest-frame and normalized to the same noise level, calculated according to Equation 2, to ensure balanced weights. A linear continuum is then subtracted from each spectrum before the residual spectra are stacked to obtain the mean spectrum. Results from 100 bootstrap realizations of the stacking procedure are shown in Figure 7. The black and red lines show the stackings of all [Ne V] λ 3426 undetected spectra in the Donley and Lacy wedges, respectively. The [Ne V] λ 3346,3426 doublet is clearly detected with mean SNR > 10 . After excluding the broad line AGNs, the stacking of Donley candidates shows that the mean SNR is 1.7 in the [Ne V] λ 3426 line region (blue line in Figure 7). The reliability of the latter stacking is limited by the small sample size (only 54 objects are included). The magenta line shows that the stacking of Lacy candidates without broad lines does feature [Ne V] λ 3426 emission (SNR \sim 2.6). Finally, the spectral stack of objects outside Lacy’s wedge (shown as the green line) does not show a clear detection (the SNR is only 1.7). This indicates a lack of AGN activity. In summary, our stacking results confirm that AGN activity exists in the MIR color-selected AGN candidates, although their low [Ne V] λ 3426 SNR implies that the emission line cannot be detected in every of the individual optical spectra.

5. AGN DECOMPOSITION IN THE MIR

Although the stacked spectra of wedge-selected AGN candidates do reveal [Ne V] λ 3426 signals, confirming their AGN activity, it is still unclear what the quantitative level of AGN activity in individual galaxies is. In this section, we develop a novel method to decompose the AGN and star formation components in the MIR. Separating the AGN emission from the host galaxy is a crucial issue in studies of the AGN-galaxy connection, particularly for Type I AGNs (Ciesla et al. 2015). Several attempts have been made to construct AGN models by solving the radiative transfer equation (Fritz et al.

¹ Hereafter we regard the objects selected by MIR color criteria but not confirmed by their spectra as AGN candidates.

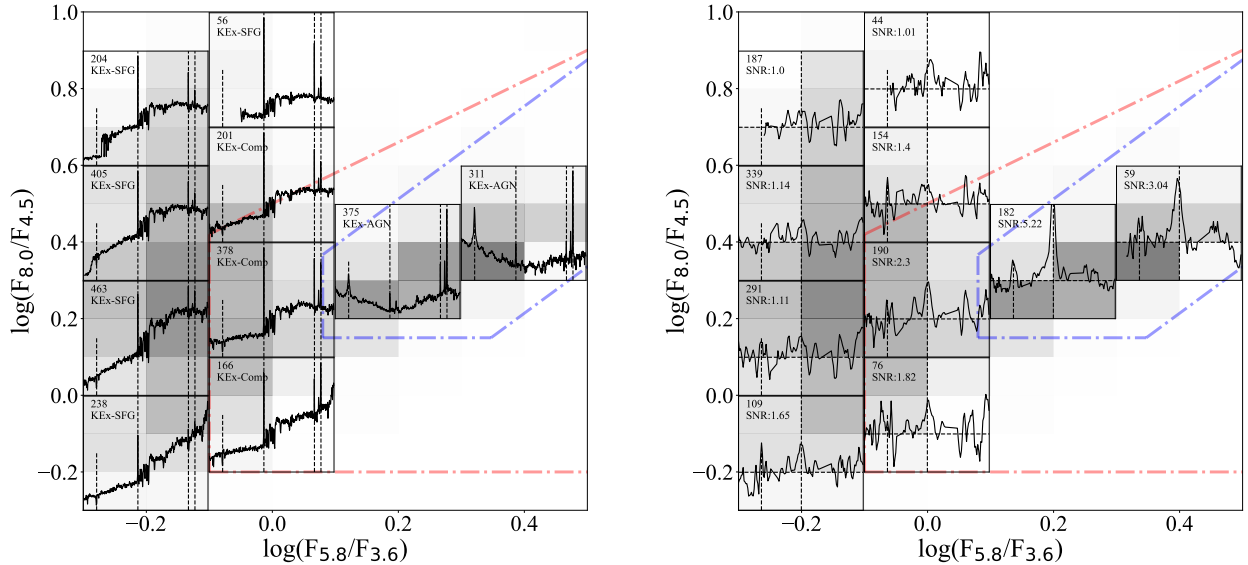


Figure 6. *Left panel:* Median composite spectra for objects binned by their location in the MIR color-color diagram. No redshift limit is applied in this panel. The rest-wavelength range of every inset panel is $2500\text{-}5200\text{\AA}$. The number of combined spectra is marked. Besides, we mark KEx classification of each spectra in the upper left corner of each inset panel. The dashed lines mark Mg II λ 2800, [O II] λ 3727, H β and [O III] λ 5007 spectral lines from left to right, respectively. *Right panel:* Mean stacking of the [Ne V] λ 3426 line region. In this panel, we only included spectra with $0.13 < z < 1.40$. The rest-wavelength range of every inset panel is $3300\text{-}3550\text{\AA}$. Two vertical dashed lines show the locations of the [Ne V] λ 3346,3426 doublet. The number of spectra used in the stacking and the SNR of stacked [Ne V] λ 3426 is marked in the upper left corner of each inset panel. The background greynshades in both panels depict the distribution of the whole $24\text{ }\mu\text{m}$ bright spectroscopic sample. The red and blue dash-dotted lines represent the Lacy and Donley wedges, respectively.

2006; Stalevski et al. 2012, 2016). Multiwavelength SED fitting codes that utilize these models have been developed (e.g., Boquien et al. 2019; Yang et al. 2020). However, these methods often require high SNR photometry across all wavelengths, which can be challenging to obtain, particularly in the far-infrared (FIR) regime. Given our lack of high quality data in the FIR, MIR colors are adopted.

We firstly apply a K-correction to calculate, for each source, three monochromatic luminosities at rest-frame wavelengths of $1.6\text{ }\mu\text{m}$, $4.5\text{ }\mu\text{m}$ and $12\text{ }\mu\text{m}$, denoted as $L_{1.6}$, $L_{4.5}$ and L_{12} , respectively. We base our K-corrections on the best-fitting MIR SED template, where this best-fitting template was identified by contrasting the observed $3.6\text{ - }24\text{ }\mu\text{m}$ photometry to each of the (redshifted and normalized) templates. To this end, we employ as template library an atlas of UV-MIR SEDs for nearby galaxies by Brown et al. (2014), which comprises 129 SEDs and covers diverse galaxy types. We further complement the SED library with 113 AGN templates from Brown et al. (2019). We take the nearest observed-frame fluxes as input to the K correction procedure. For example, if an object has a redshift of $z = 0.5$, the rest $4.5\text{ }\mu\text{m}$ emission is redshifted to $6.75\text{ }\mu\text{m}$, in which case we use observed $5.8\text{ }\mu\text{m}$ flux (nearest to $6.75\text{ }\mu\text{m}$) to K-correct to get rest $L_{4.5}$. In practice,

across the variety of sources represented in our sample, the contributions from AGN and non-AGN components to the MIR luminosities will vary. The latter in principle can comprise both direct emission from stars (taken to dominate the $1.6\text{ }\mu\text{m}$ emission) and dust-reprocessed emission from star formation (more important at longer wavelengths). In an effort to disentangle these different components, we adopt the following decomposition method. For rest-frame $L_{4.5}$, the emission could originate from AGN-heated dust, stellar emission, and star-forming emission. For L_{12} , the stellar emission is expected to be negligible. In our analysis, we treat the derived $L_{4.5}$ and L_{12} as the sum of AGN and non-AGN components,

$$L_{4.5} = L_{4.5}^* + L_{4.5}^{AGN}, \quad (3)$$

and

$$L_{12} = L_{12}^* + L_{12}^{AGN}, \quad (4)$$

We assume that the AGN emission in the MIR follows a power law distribution, which is an approach commonly used in the literature to describe the continuum emission of AGNs in this wavelength range (e.g., Mullaney et al. 2011; Casey 2012; Bernhard et al. 2021),

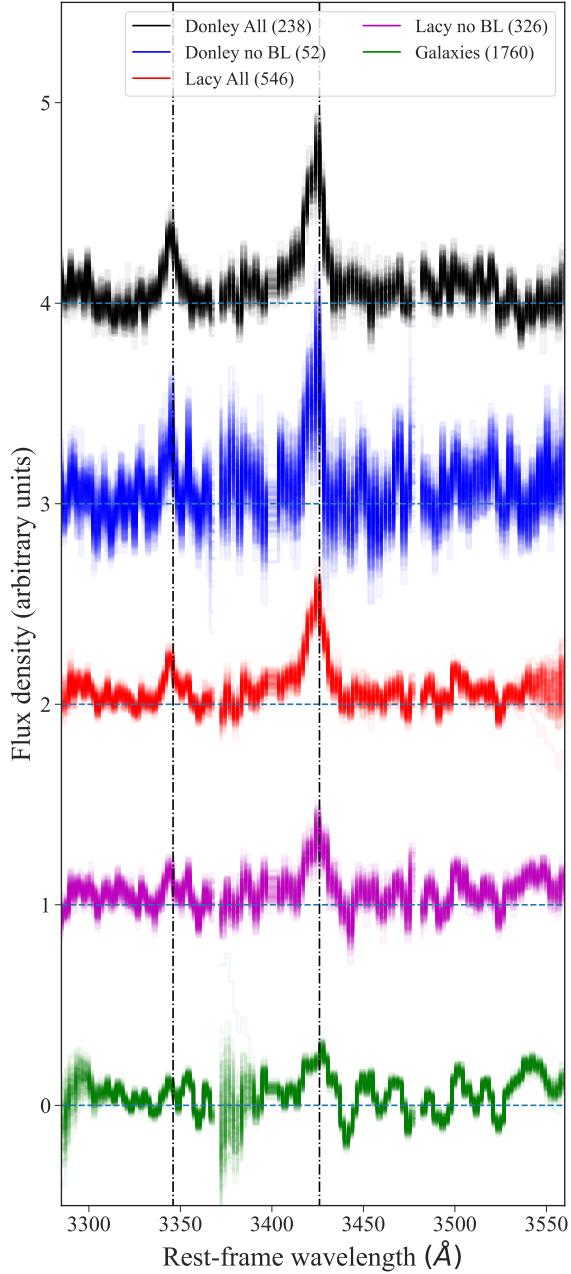


Figure 7. Mean spectral stacks near the $[\text{Ne V}]\lambda 3426$ line region. The 88 AGNs that have individual $[\text{Ne V}]\lambda 3426$ detections are not included. The red and black lines are stackings of AGN candidates selected by the Lacy and Donley wedges, respectively. The magenta and blue lines are the corresponding stacks after removal of objects with broad line features. A stack of $24\mu\text{m}$ selected sources outside the Lacy wedge is shown in green. The number of spectra entering each stack are labeled in the legend.

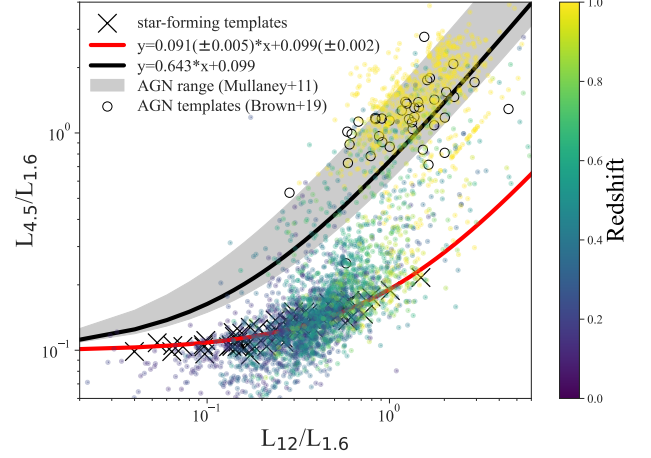


Figure 8. L_{12} vs $L_{4.5}$. Parameters are normalized to $L_{1.6}$ to avoid correlation caused by redshift. Black crosses are the star forming templates from (Huang et al. 2021), with the red line showing a linear fit to them. The color bar indicates redshift. The black open circles are AGN templates from Brown et al. (2019). The grey-shaded region shows the range of α values from Mullaney et al. (2011). In this figure, we only include 3679 objects ($\sim 91\%$ of the whole spectroscopic sample) that have photometry in at least three bands from 3.6 to $24\mu\text{m}$.

$$L_{12}^{AGN} = (12/4.5)^\alpha L_{4.5}^{AGN}, \quad (5)$$

Huang et al. (2021) performed further classification of the SED atlas by Brown et al. (2014) into 5 populations based on MIR color and the EW of a polycyclic aromatic hydrocarbon (PAH) feature. The resulting 5 populations were labelled AGN, star forming, composite, quiescent, and blue compact. We derive the correlation between $L_{4.5}^*$ and L_{12}^* using their 65 star forming templates (shown as the red line in Figure 8):

$$L_{4.5}^* = 0.091(\pm 0.005)L_{12}^* + 0.099(\pm 0.002)L_{1.6}. \quad (6)$$

After combining Equations 3 to 6, we calculate $L_{4.5}^{AGN}$ as:

$$L_{4.5}^{AGN} = k(L_{4.5} - 0.091L_{12} - 0.099L_{1.6}), \quad (7)$$

where k equals $(1 - 0.091(12/4.5)^\alpha)^{-1}$. Similarly, the star formation contribution at $12\mu\text{m}$ (L_{12}^*) is given by

$$L_{12}^* = k(L_{12} - (12/4.5)^\alpha L_{4.5} + 0.099(12/4.5)^\alpha L_{1.6}). \quad (8)$$

All of the luminosities mentioned above can be determined once an appropriate value of α is adopted, parametrizing the slope of the AGN MIR SED. Dai et al. (2012) constructed the median quasar SED based on the

same $24\ \mu\text{m}$ bright sample, and they found that α equals 0.45 and k equals 1.16. Other studies, such as those by [Mullaney et al. \(2011\)](#), show that the AGN SEDs have α values between -0.3 and 0.7, which translates to k values between 1.07 and 1.22. Here we use α equals 0.45 to calculate the luminosities mentioned above, for consistency with [Dai et al. \(2012\)](#) whose sample is comprised within ours. We also consider α values between -0.3 and 0.7 to calculate the lower and upper limits to AGN luminosity for each object, respectively. As shown in the Figure 8, the AGN templates from [Brown et al. \(2019\)](#) are consistent with the α range between -0.3 and 0.7. This result reinforces our determination of α values.

Equation 8 would result in a negative value when $L_{12}/L_{1.6} < (12/4.5)^\alpha (L_{4.5}/L_{1.6} - 0.099)$. That would convey an AGN luminosity at $12\ \mu\text{m}$ exceeding the total $12\ \mu\text{m}$ luminosity, which is unphysical. We therefore consider such extreme objects as having their $12\ \mu\text{m}$ emission entirely dominated by the AGN. Along a similar vein, the objects located below the red line are treated as pure star-forming galaxies. This approach enables us to calculate the AGN fraction in a single band for every object.

To verify our method, we also do multiwavelength SED fitting for our objects from the optical to the FIR wavebands. The photometries we used are listed in the Table 1. The fitting is done by CIGALE code ([Boquien et al. 2019; Yang et al. 2020](#)), which includes a AGN component in the fitting. We compare the L_{12}^{AGN} from our method and that from multiwavelength SED fitting, see Figure 9. We label the objects that have $\text{SNR} > 3$ in at least 3 FIR bands from 100 to $500\ \mu\text{m}$ as ‘‘FIR detected’’. The label indicates the objects with reliable FIR fitting. As shown in the Figure 9, we find the consistency between our method and SED fitting for both ‘‘FIR detected’’ and ‘‘FIR undetected’’ subsamples. We further investigate the reliability of SF luminosity that we derived, see Section 6.2.

With the monochromatic rest-frame luminosities in hand, we first construct and investigate $[\text{Ne V}]\lambda 3426$ stacks for subsets of MIR-selected sources binned by their L_{12} luminosity (see left panel of Figure 10). We find that with greater L_{12} luminosity comes stronger $[\text{Ne V}]\lambda 3426$ emission. The spectra of AGNs with $L_{12} > 10^{43.5}$ erg/s (two upper panels) display distinct $[\text{Ne V}]\lambda 3426$ emission. However, for mid-to-low luminosity objects ($L_{12} < 10^{43.5}$ erg/s), the SNRs of $[\text{Ne V}]\lambda 3426$ are lower than 2. This finding is consistent with previous studies on $[\text{Ne V}]\lambda 14.3\ \mu\text{m}$ based on *Spitzer*/IRS spectra. Specifically, [Dasyra et al. \(2008\)](#) show that $[\text{Ne V}]\lambda 14.3\ \mu\text{m}$ emission is stronger in Type I AGNs with higher luminosities. In our work, we did

not differentiate between the Type I/II nature of AGNs and find the same result. Besides, in the right panel of Figure 10, we plot AGN fraction at $12\ \mu\text{m}$ against $12\ \mu\text{m}$ total luminosity. The AGN fraction increases along with the increasing $12\ \mu\text{m}$ luminosity. These result from Figure 10 demonstrate that more luminous MIR sources tend to host more prominent AGN activity.

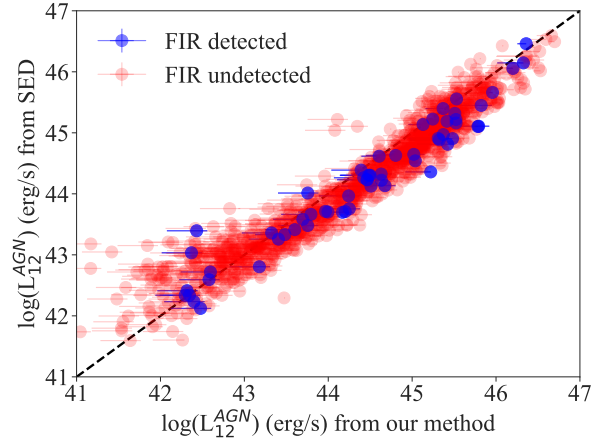


Figure 9. Comparison of $12\ \mu\text{m}$ AGN luminosities derived from our method and those from SED fitting. The red dots are FIR undetected objects and the blue dots are FIR detected objects. The black dashed line shows 1:1 correlation. A good consistency is found between these two methods for AGN decomposition.

We also generate composite spectra based on the positions of the sources in Figure 8, following the same procedures described in Section 4.1. The results are presented in Figure 11. Every inset panel in this figure corresponds to a bin of 0.5 dex in $L_{12}/L_{1.6}$ and 0.5 dex in $L_{4.5}/L_{1.6}$. Type I quasar features (e.g., broad Mg II lines) are clearly visible in the $(10^0, 10^0)$ and $(10^{-0.5}, 10^{-0.5})$ bins. However, spectra in the $(10^{-0.5}, 10^{-0.5})$ bin have a redder continuum, indicating a transitional state between Type I and Type II. Spectra in the $(10^0, 10^{-0.5})$ bin exhibit Type II quasar features (narrow permitted lines and flat continua). Consistently, $[\text{Ne V}]\lambda 3426$ stacking reveals detections in all these three bins. Comparing these three composite spectra, we find that Type II AGNs usually have lower $L_{4.5}$ and higher L_{12} compared with Type I AGNs, normalized by $L_{1.6}$. This conclusion suggests that Type I AGNs are usually bluer and Type II are redder (‘‘rising’’) even in the MIR regime. Previous studies arrived at consistent conclusions (e.g., [Ogawa et al. 2021](#)). By definition, Type II AGNs are obscured objects, by dust and gas from either the circumnuclear region or the interstellar medium (ISM) on the galactic scale. If the obscuration is from the ISM, the extinction (typically $A_V \sim 0-2$ mag,

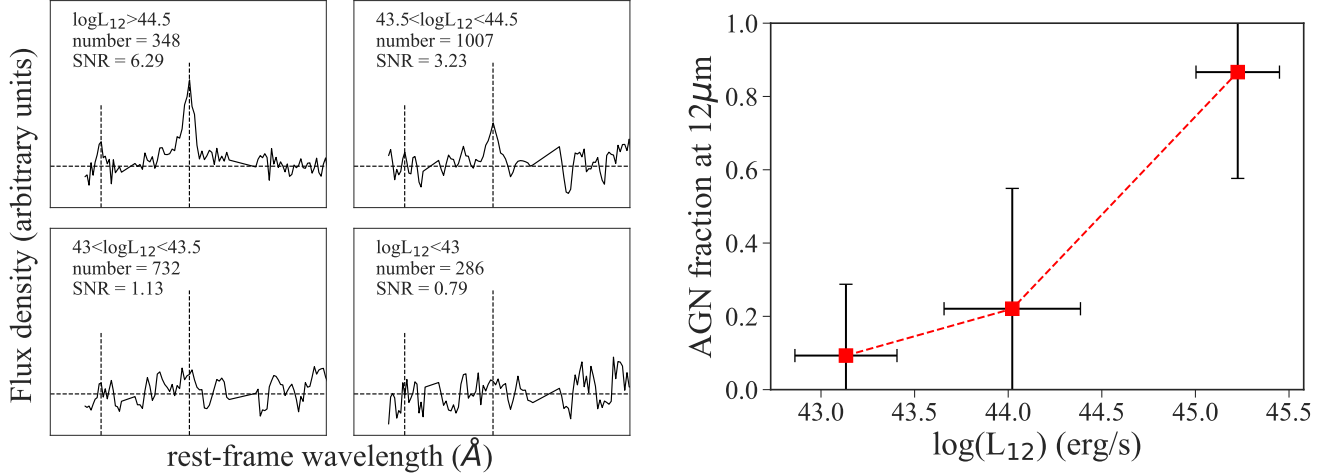


Figure 10. *Left Panel:* Mean spectral stacks of the [Ne V] λ 3426 line region for different $12\mu\text{m}$ total luminosities. Luminosity ranges, number of spectra and stacked SNR in each bin are marked in each panel. More luminous objects feature the stronger [Ne V] λ 3426 emission. *Right Panel:* AGN fraction at $12\mu\text{m}$ versus $12\mu\text{m}$ total luminosity. More luminous objects tend to have higher AGN fractions.

see e.g., Cid Fernandes et al. 2005) would result in a redder optical-NIR SED. However, it should not affect the MIR SED since the obscuring material is optically thin in the MIR (Donley et al. 2012).

On the other hand, central obscuration near the nucleus could also result in the observed difference in the SEDs of Type I and II AGNs. Nevertheless, the circumnuclear extinction may not explain the difference of MIR SED shapes in the majority of AGNs ($\log N_H \sim 20$ – 24 cm^{-2}), as it was found that the SEDs do not change significantly across a wide range of circumnuclear extinction, with $\log N_H$ values from 20 to 24 cm^{-2} (see Figure 15 in Bernhard et al. 2021), even after correcting for the silicate absorption at $9.7\mu\text{m}$ that dominates the ISM (e.g., Goulding et al. 2012). As an alternative explanation, Bernhard et al. (2021) argued that the “intrinsic” rising SED may arise from complex nuclear dusty structures such as extended polar dust (see Ogawa et al. 2021). In these heavily obscured systems (e.g., Compton-thick systems with $\log N_H > 24\text{ cm}^{-2}$), the hot dust emission from the nuclear region is partly absorbed by the extended dust components and re-emitted at longer wavelengths, leading to a cooler (and thus redder in the MIR) SED.

6. AGN AND STAR FORMATION

6.1. AGN bolometric luminosity

In this study, we use the monochromatic calibration described in Runnoe et al. (2012):

$$\log(L_{bol}^{AGN}) = 0.822(\pm 0.096) \log(L_{12}^{AGN}) + 8.915(\pm 4.303), \quad (9)$$

to convert L_{12}^{AGN} into AGN bolometric luminosity.

6.2. Star formation rate

The conversion of MIR monochromatic luminosity to star formation rate (SFR) has been explored in several studies (e.g., Calzetti et al. 2007; Rieke et al. 2009). In this study, we use the calibration presented in Lee et al. (2013) to estimate SFR from $12\mu\text{m}$ luminosity, in units of M_{\odot}/yr :

$$\log(SFR_{12}) = 1.03 \log(L_{12}^*) - 43.77. \quad (10)$$

We also obtain FIR luminosities (the wavelength range in this work is defined as 40 – $500\mu\text{m}$) by fitting the templates from Chary & Elbaz (2001) to approximately 20% of our objects (those that have $\text{SNR} > 3$ in at least 3 FIR bands from 100 to $500\mu\text{m}$, see Table 1). We then convert the FIR luminosities to SFRs using:

$$\log(SFR_{FIR}) = 1.02 \log(L_{FIR}) - 44.42. \quad (11)$$

This equation is originally from Kennicutt (1998). We find a good agreement between the SFRs derived from the $12\mu\text{m}$ luminosity and the FIR luminosity, see Figure 12. This result is also consistent with the expectations from star-forming templates (Rieke et al. 2009), which further confirms our MIR-based SFR estimate.

As a sanity check, we also stacked the [Ne V] λ 3426 spectra based on the ratio between the total $12\mu\text{m}$ luminosity and their FIR luminosity. Figure 13, the objects featuring the strongest MIR emission relative to their FIR output tend to be associated with a stronger [Ne V] signal, indicative of their MIR excess being due to stronger AGN activity.

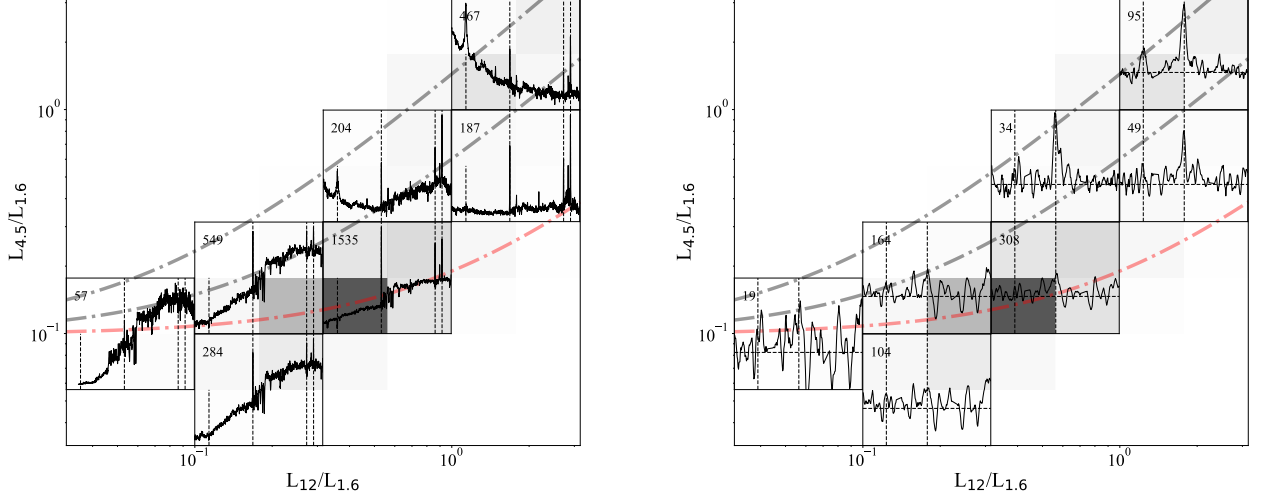


Figure 11. *Left panel:* Composite spectra across the $L_{12}/L_{1.6}$ versus $L_{4.5}/L_{1.6}$ diagram. No redshift limit was applied in this panel. The rest-wavelength range of every inset panel is 2500-5200Å. The number of combined spectra is marked. Besides, we mark KEx classification of each spectra in the upper left corner of each inset panel. The dashed lines mark Mg II λ 2800, [O II] λ 3727, H β and [O III] λ 5007 spectral lines from left to right, respectively. *Right panel:* Mean stacking of the [Ne V] λ 3426 line region. In this panel, we only included spectra with $0.13 < z < 1.40$. The wavelength range of every inset panel is 3300-3550Å. Two vertical dashed lines show the location of the [Ne V] λ 3426,3426 doublet. The number of spectra used in the stacking and the SNR of stacked [Ne V] λ 3426 is marked in the upper left corner of each inset panel. The red dash-dotted lines in both panels show pure star formation relations while the black dash-dotted show the range of α values we adopt.

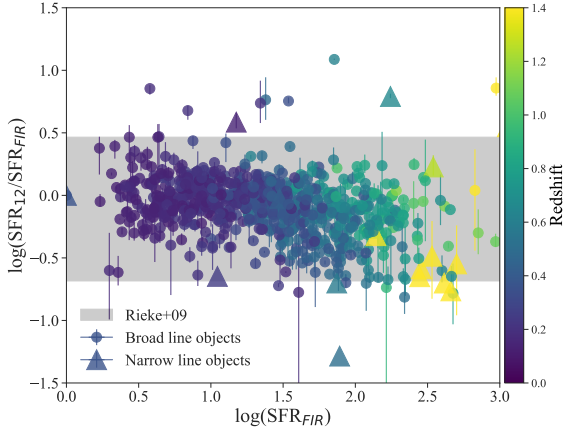


Figure 12. Comparison of SFRs derived from $12\mu\text{m}$ and those from FIR emission. Triangles mark broad line objects and dots are narrow line objects. The grey-shaded shows the template prediction of SEDs from Rieke et al. (2009).

6.3. Correlation between AGN and star formation

The relation between AGN luminosity and star formation rate has been extensively studied (Rosario et al. 2012; Azadi et al. 2015; Shimizu et al. 2017; Dai et al. 2018; Jackson et al. 2020). Theoretical models suggest that the star formation activities and AGN activities in galaxies may be related (Di Matteo et al. 2005; Hopkins et al. 2006). Gas infall can trigger both AGN and star

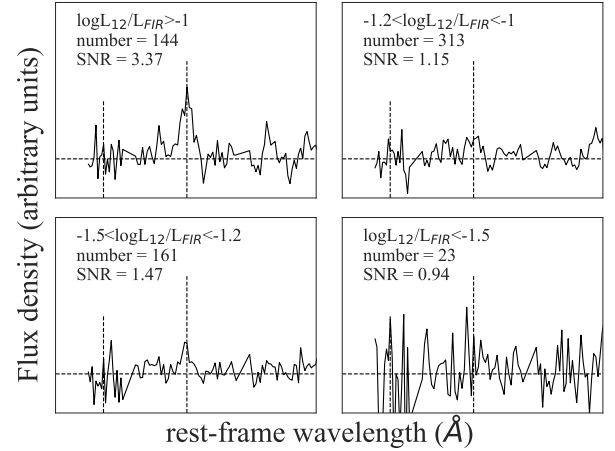


Figure 13. Mean spectral stacks of the [Ne V] λ 3426 line region for different L_{12}/L_{FIR} ratios. The range of the considered luminosity ratio, number of spectra and stacked SNR in each bin are marked in each panel. Objects which are more luminous at $12\mu\text{m}$ compared with the FIR have the stronger [Ne V] λ 3426 emission.

formation (Somerville et al. 2008), while AGN feedback can suppress star formation in the host galaxy (Springel et al. 2005). Observational studies have shown a positive relationship between AGN and star formation in some cases (Lutz et al. 2008; Chen et al. 2013; Dai et al. 2018), while in other studies, the relationship becomes weak or absent (Shao et al. 2010; Harrison et al. 2012;

Barger et al. 2015; Bernhard et al. 2016; Shimizu et al. 2017). Shao et al. (2010) proposed a two-phase model where, for low luminosity AGNs, the AGN-SF relation is weak, reflecting a secular evolutionary path, whereas for high luminosity AGNs, the AGN and star formation in the host galaxy are linked due to the merging process, boosting both. The relationship between AGN and star formation is further complicated by the different timescales of AGN and star formation activities. Hickox et al. (2014) considered the variability of AGNs and found a consistent AGN-SF relation with the two-phase model proposed by Shao et al. (2010).

Figure 14 shows the SFR as a function of AGN luminosity, along with the relations from Netzer (2009), Hickox et al. (2014), and Dai et al. (2018). The red dashed line represents the linear fit to our parent spectroscopic sample showing a positive relation between AGN and star formation activities. We note that only 1811 objects with measurements of both L_{bol}^{AGN} and SFR are included, and objects below the red line (i.e. pure star-forming galaxies) and above the black line (i.e. pure AGNs) in Figure 8 are excluded. Nevertheless, a larger sample of less luminous AGNs with $\log L_{bol}^{AGN} < 43$ erg/s is required to confirm the possible flattening of the AGN-SF relation at the low luminosity end. It is worth noting that the sample selection could affect the linear relation shown in Figure 14. For example, Dai et al. (2018) studied an FIR-bright quasar sample at similar redshifts, while Netzer (2009) focused on a local SDSS AGN sample. These differences could explain that our sample lies in between the two referenced relations. The lower fraction of FIR-bright objects could explain our lower SFR than Dai et al. (2018), while the higher redshift in our sample, as well as the $24\mu\text{m}$ selection result in the higher SFR compared to Netzer (2009). As a cautionary note, we emphasize that our sample comprises AGNs spanning a wide range in lookback times, and higher-redshift galaxies are well known to host larger gas reservoirs and feature higher SFRs. Therefore, population effects, stemming from the broad range in galaxy properties and redshifts included within the sample, may contribute to shaping the relation seen in Figure 14. The presence of an L_{bol}^{AGN} – SFR correlation may thus not necessarily be taken as a direct imprint of individual galaxies experiencing temporal co-evolution. We illustrate the redshift distribution of sources across the L_{bol}^{AGN} – SFR diagram in the right panel of Figure 14. At $L_{bol}^{AGN} < 10^{45}$ erg/s, higher redshift objects are seen to feature higher SFR. This reflects the redshift evolution of the SF main sequence (Schreiber et al. 2015, e.g.,). The SFR shows a weaker dependency on the AGN luminosity for objects at similar redshift. The lack of a strong L_{bol}^{AGN} – SFR

relation once controlling for redshift is also reported by Stanley et al. (2015), who apply an X-ray AGN selection and luminosity measurement. Due to the variability of AGNs, the measurement of SFR and L_{bol}^{AGN} is sensitive to the time scale of the relevant physical processes. Short time-scale variations in such systems could flatten the relationship between SFR and L_{bol}^{AGN} (Stanley et al. 2015). Other factors such as location of SF activity could also wash out the relationship (Volonteri et al. 2015). Broad line objects dominate the population with $L_{bol}^{AGN} > 10^{45}$ erg/s and they occupy the high-SFR and high- L_{bol}^{AGN} space of Figure 14. They show a strong L_{bol}^{AGN} – SFR relation. Based on X-ray data, Rosario et al. (2012) found the same conclusion that the black hole activity tracks global SF of the host galaxy in high luminosity AGNs. They argued that this connection could result from rapid gas inflow associated with mergers. The gas inflow fuels both AGN accretion and nuclear star-formation. Thus the L_{bol}^{AGN} – SFR relation in our sample could stem partly from such interconnection, with additional contributions from the varying population properties across the range of redshifts explored.

7. CONCLUSION

We present an optical spectroscopic sample of $24\mu\text{m}$ bright objects in the Lockman Hole field from the SWIRE survey, obtained with MMT/Hectospec. Out of all targets with $F_{24} > 400\mu\text{Jy}$ and $17.7 < r < 22.5$, $\sim 54\%$ is covered in our sample. The sample is further supplemented with optically bright ($r < 17.7$) sources above the same $24\mu\text{m}$ threshold with spectra from SDSS. Given the redshift distribution of our sample, we used [Ne V] $\lambda 3426$ as the preferred diagnostic to evaluate the presence of AGNs in the 4035 spectra with $z > 0.13$, and identified 88 robust [Ne V] $\lambda 3426$ -selected AGNs with $\text{SNR} > 3$. We combined the sample with previously identified Type I broad-line AGNs, together yielding a total sample of 887 AGNs (844 of them are Type I AGNs).

Compared with various AGN MIR color selections, we confirm that 53% of objects selected by the Lacy color criteria are also spectrally confirmed AGNs. The percentage increases to 84% for the Donley wedge.

To determine the potential AGN activity within [Ne V] $\lambda 3426$ undetected, wedge-selected AGN candidates, we stack their spectra to look for [Ne V] $\lambda 3426$ emission. We find that the stacked [Ne V] $\lambda 3426$ strength increases with increasing $12\mu\text{m}$ luminosity, indicating that the most MIR luminous objects tend to host more prominent AGN activity. This result is also consistent with the conclusion from our decomposition, which reveals that objects with greater $12\mu\text{m}$ luminosity have larger AGN fraction.

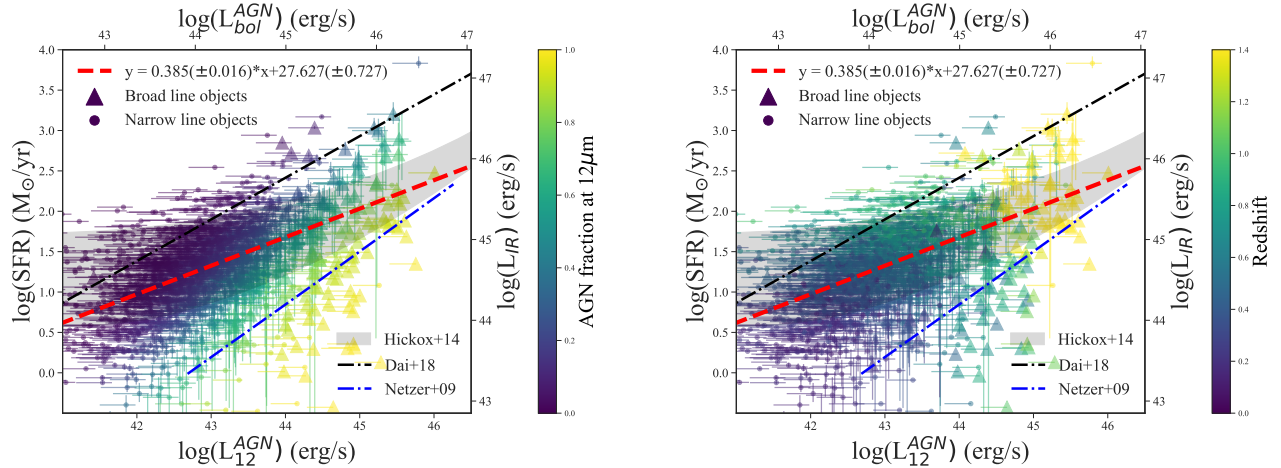


Figure 14. SFR versus AGN $12\mu\text{m}$ luminosity. Colors are AGN fraction at $12\mu\text{m}$ and redshift in the left and right panels, respectively. Triangles mark broad line objects and dots are narrow line objects. The red dashed line is a linear fit to all objects with SFR and AGN luminosity measurements (1811 objects, see Section 5). Fitting parameters are listed in the upper left legend. The blue dash-dotted line is the relation found by Netzer (2009). The black dash-dotted line is the relation derived by Dai et al. (2018). The grey polygon shows the model prediction from Hickox et al. (2014). The bolometric luminosities are converted from L_{12}^{AGN} using the correction described in Runnoe et al. (2012).

The stacking of both Lacy and Donley candidates in the $[\text{Ne V}]\lambda 3426$ region shows clear detections. Our stacking analysis confirms that AGN activity is present among MIR color-selected AGN candidates, although their low SNR $[\text{Ne V}]\lambda 3426$ cannot be detected in all of the individual optical spectra.

To quantify the AGN and star forming contribution in each object, we develop a novel method to decompose the AGN and star formation components in the MIR. The relation between SFR and AGN bolometric luminosity of our sample is consistent with the two-phase model prediction over a dynamic range in L_{bol}^{AGN} of 10^{43} to 10^{47} erg/s. We discuss that part of this correlation is attributed to the higher-redshift objects in our sample populating the more luminous L_{bol}^{AGN} and higher SFR regime.

In summary, our study confirms spectroscopically the presence of AGN activity in MIR color-selected AGN candidates. The AGN strength is larger in the more luminous MIR sources. We develop a novel method to decompose the AGN and star formation contribution

using rest-frame MIR colors. Based on this method, we find a positive correlation between AGN luminosity and SFR.

The authors would like to thank Cheng Cheng, Hai Xu, Piaoran Liang, Yaru Shi, Shumei Wu, Gabriel Oio and Xianzhong Zheng for helpful discussions. This work is sponsored by the National Key R&D Program of China for grant No. 2022YFA1605300, the National Nature Science Foundation of China (NSFC) grants No. 12273051 and 11933003. The authors gratefully acknowledge support from the Royal Society International Exchanges Scheme (IES\R1\211140) and the Chinese Academy of Sciences President's International Fellowship Initiative (grant no. 2022VMB0004). T. C. acknowledges the China Postdoctoral Science Foundation (Grant No. 2023M742929). Additional support came from the Chinese Academy of Sciences (CAS) through a grant to the South America Center for Astronomy (CASSACA) in Santiago, Chile.

REFERENCES

- Abdurro'uf, Accetta, K., Aerts, C., et al. 2022, ApJS, 259, 35, doi: [10.3847/1538-4365/ac4414](https://doi.org/10.3847/1538-4365/ac4414)
- Abel, N. P., & Satyapal, S. 2008, ApJ, 678, 686, doi: [10.1086/529013](https://doi.org/10.1086/529013)
- Alonso-Herrero, A., Pérez-González, P. G., Alexander, D. M., et al. 2006, ApJ, 640, 167, doi: [10.1086/499800](https://doi.org/10.1086/499800)
- Assef, R. J., Kochanek, C. S., Brodwin, M., et al. 2010, ApJ, 713, 970, doi: [10.1088/0004-637X/713/2/970](https://doi.org/10.1088/0004-637X/713/2/970)
- Assef, R. J., Stern, D., Kochanek, C. S., et al. 2013, ApJ, 772, 26, doi: [10.1088/0004-637X/772/1/26](https://doi.org/10.1088/0004-637X/772/1/26)
- Azadi, M., Aird, J., Coil, A. L., et al. 2015, ApJ, 806, 187, doi: [10.1088/0004-637X/806/2/187](https://doi.org/10.1088/0004-637X/806/2/187)

- Baldwin, J. A., Phillips, M. M., & Terlevich, R. 1981, *PASP*, 93, 5, doi: [10.1086/130766](https://doi.org/10.1086/130766)
- Barger, A. J., Cowie, L. L., Owen, F. N., et al. 2015, *ApJ*, 801, 87, doi: [10.1088/0004-637X/801/2/87](https://doi.org/10.1088/0004-637X/801/2/87)
- Bernhard, E., Mullaney, J. R., Daddi, E., Ciesla, L., & Schreiber, C. 2016, *MNRAS*, 460, 902, doi: [10.1093/mnras/stw973](https://doi.org/10.1093/mnras/stw973)
- Bernhard, E., Tadhunter, C., Mullaney, J. R., et al. 2021, *MNRAS*, 503, 2598, doi: [10.1093/mnras/stab419](https://doi.org/10.1093/mnras/stab419)
- Boquien, M., Burgarella, D., Roehlly, Y., et al. 2019, *A&A*, 622, A103, doi: [10.1051/0004-6361/201834156](https://doi.org/10.1051/0004-6361/201834156)
- Bower, R. G., Benson, A. J., Malbon, R., et al. 2006, *MNRAS*, 370, 645, doi: [10.1111/j.1365-2966.2006.10519.x](https://doi.org/10.1111/j.1365-2966.2006.10519.x)
- Brown, M. J. I., Duncan, K. J., Landt, H., et al. 2019, *MNRAS*, 489, 3351, doi: [10.1093/mnras/stz2324](https://doi.org/10.1093/mnras/stz2324)
- Brown, M. J. I., Moustakas, J., Smith, J. D. T., et al. 2014, *ApJS*, 212, 18, doi: [10.1088/0067-0049/212/2/18](https://doi.org/10.1088/0067-0049/212/2/18)
- Calzetti, D., Kennicutt, R. C., Engelbracht, C. W., et al. 2007, *ApJ*, 666, 870, doi: [10.1086/520082](https://doi.org/10.1086/520082)
- Casey, C. M. 2012, *MNRAS*, 425, 3094, doi: [10.1111/j.1365-2966.2012.21455.x](https://doi.org/10.1111/j.1365-2966.2012.21455.x)
- Chary, R., & Elbaz, D. 2001, *ApJ*, 556, 562, doi: [10.1086/321609](https://doi.org/10.1086/321609)
- Chen, C.-T. J., Hickox, R. C., Alberts, S., et al. 2013, *ApJ*, 773, 3, doi: [10.1088/0004-637X/773/1/3](https://doi.org/10.1088/0004-637X/773/1/3)
- Cid Fernandes, R., Mateus, A., Sodré, L., Stasińska, G., & Gomes, J. M. 2005, *MNRAS*, 358, 363, doi: [10.1111/j.1365-2966.2005.08752.x](https://doi.org/10.1111/j.1365-2966.2005.08752.x)
- Ciesla, L., Charmandaris, V., Georgakakis, A., et al. 2015, *A&A*, 576, A10, doi: [10.1051/0004-6361/201425252](https://doi.org/10.1051/0004-6361/201425252)
- Ciotti, L., Ostriker, J. P., & Proga, D. 2010, *ApJ*, 717, 708, doi: [10.1088/0004-637X/717/2/708](https://doi.org/10.1088/0004-637X/717/2/708)
- Civano, F., Marchesi, S., Comastri, A., et al. 2016, *ApJ*, 819, 62, doi: [10.3847/0004-637X/819/1/62](https://doi.org/10.3847/0004-637X/819/1/62)
- Cleri, N. J., Yang, G., Papovich, C., et al. 2022, arXiv e-prints, arXiv:2209.06247. <https://arxiv.org/abs/2209.06247>
- Cresci, G., Mainieri, V., Brusa, M., et al. 2015, *ApJ*, 799, 82, doi: [10.1088/0004-637X/799/1/82](https://doi.org/10.1088/0004-637X/799/1/82)
- Croton, D. J., Springel, V., White, S. D. M., et al. 2006, *MNRAS*, 365, 11, doi: [10.1111/j.1365-2966.2005.09675.x](https://doi.org/10.1111/j.1365-2966.2005.09675.x)
- Dai, Y. S., Wilkes, B. J., Bergeron, J., et al. 2018, *MNRAS*, 478, 4238, doi: [10.1093/mnras/sty1341](https://doi.org/10.1093/mnras/sty1341)
- Dai, Y. S., Bergeron, J., Elvis, M., et al. 2012, *ApJ*, 753, 33, doi: [10.1088/0004-637X/753/1/33](https://doi.org/10.1088/0004-637X/753/1/33)
- Dai, Y. S., Elvis, M., Bergeron, J., et al. 2014, *ApJ*, 791, 113, doi: [10.1088/0004-637X/791/2/113](https://doi.org/10.1088/0004-637X/791/2/113)
- Dasyra, K. M., Ho, L. C., Armus, L., et al. 2008, *ApJL*, 674, L9, doi: [10.1086/528843](https://doi.org/10.1086/528843)
- Di Matteo, T., Springel, V., & Hernquist, L. 2005, *Nature*, 433, 604, doi: [10.1038/nature03335](https://doi.org/10.1038/nature03335)
- Donley, J. L., Rieke, G. H., Pérez-González, P. G., Rigby, J. R., & Alonso-Herrero, A. 2007, *ApJ*, 660, 167, doi: [10.1086/512798](https://doi.org/10.1086/512798)
- Donley, J. L., Koekemoer, A. M., Brusa, M., et al. 2012, *ApJ*, 748, 142, doi: [10.1088/0004-637X/748/2/142](https://doi.org/10.1088/0004-637X/748/2/142)
- Fabian, A. C. 2012, *ARA&A*, 50, 455, doi: [10.1146/annurev-astro-081811-125521](https://doi.org/10.1146/annurev-astro-081811-125521)
- Farrah, D., Afonso, J., Efstathiou, A., et al. 2003, *MNRAS*, 343, 585, doi: [10.1046/j.1365-8711.2003.06696.x](https://doi.org/10.1046/j.1365-8711.2003.06696.x)
- Ferrarese, L., & Merritt, D. 2000, *ApJL*, 539, L9, doi: [10.1086/312838](https://doi.org/10.1086/312838)
- Fritz, J., Franceschini, A., & Hatziminaoglou, E. 2006, *MNRAS*, 366, 767, doi: [10.1111/j.1365-2966.2006.09866.x](https://doi.org/10.1111/j.1365-2966.2006.09866.x)
- Gebhardt, K., Bender, R., Bower, G., et al. 2000, *ApJL*, 539, L13, doi: [10.1086/312840](https://doi.org/10.1086/312840)
- Gilli, R., Vignali, C., Mignoli, M., et al. 2010, *A&A*, 519, A92, doi: [10.1051/0004-6361/201014039](https://doi.org/10.1051/0004-6361/201014039)
- Goulding, A. D., Alexander, D. M., Bauer, F. E., et al. 2012, *ApJ*, 755, 5, doi: [10.1088/0004-637X/755/1/5](https://doi.org/10.1088/0004-637X/755/1/5)
- Gültekin, K., Richstone, D. O., Gebhardt, K., et al. 2009, *ApJ*, 698, 198, doi: [10.1088/0004-637X/698/1/198](https://doi.org/10.1088/0004-637X/698/1/198)
- Hainline, K. N., Hickox, R. C., Carroll, C. M., et al. 2014, *ApJ*, 795, 124, doi: [10.1088/0004-637X/795/2/124](https://doi.org/10.1088/0004-637X/795/2/124)
- Hao, L., Strauss, M. A., Tremonti, C. A., et al. 2005, *AJ*, 129, 1783, doi: [10.1086/428485](https://doi.org/10.1086/428485)
- Häring, N., & Rix, H.-W. 2004, *ApJL*, 604, L89, doi: [10.1086/383567](https://doi.org/10.1086/383567)
- Harrison, C. M., Alexander, D. M., Mullaney, J. R., et al. 2012, *ApJL*, 760, L15, doi: [10.1088/2041-8205/760/1/L15](https://doi.org/10.1088/2041-8205/760/1/L15)
- Hickox, R. C., & Alexander, D. M. 2018, *ARA&A*, 56, 625, doi: [10.1146/annurev-astro-081817-051803](https://doi.org/10.1146/annurev-astro-081817-051803)
- Hickox, R. C., Mullaney, J. R., Alexander, D. M., et al. 2014, *ApJ*, 782, 9, doi: [10.1088/0004-637X/782/1/9](https://doi.org/10.1088/0004-637X/782/1/9)
- Hopkins, P. F., Hernquist, L., Cox, T. J., et al. 2006, *ApJS*, 163, 1, doi: [10.1086/499298](https://doi.org/10.1086/499298)
- Huang, J. S., Dai, Y. S., Willner, S. P., et al. 2021, *ApJ*, 912, 161, doi: [10.3847/1538-4357/abec50](https://doi.org/10.3847/1538-4357/abec50)
- Jackson, T. M., Rosario, D. J., Alexander, D. M., et al. 2020, *MNRAS*, 498, 2323, doi: [10.1093/mnras/staa2414](https://doi.org/10.1093/mnras/staa2414)
- Jin, G., Dai, Y. S., Pan, H.-A., et al. 2021, *ApJ*, 923, 6, doi: [10.3847/1538-4357/ac2901](https://doi.org/10.3847/1538-4357/ac2901)
- Juneau, S., Dickinson, M., Alexander, D. M., & Salim, S. 2011, *ApJ*, 736, 104, doi: [10.1088/0004-637X/736/2/104](https://doi.org/10.1088/0004-637X/736/2/104)
- Juneau, S., Bournaud, F., Charlot, S., et al. 2014, *ApJ*, 788, 88, doi: [10.1088/0004-637X/788/1/88](https://doi.org/10.1088/0004-637X/788/1/88)
- Kauffmann, G., Heckman, T. M., Tremonti, C., et al. 2003, *MNRAS*, 346, 1055, doi: [10.1111/j.1365-2966.2003.07154.x](https://doi.org/10.1111/j.1365-2966.2003.07154.x)

- Kennicutt, Robert C., J. 1998, *ARA&A*, 36, 189, doi: [10.1146/annurev.astro.36.1.189](https://doi.org/10.1146/annurev.astro.36.1.189)
- Kewley, L. J., Groves, B., Kauffmann, G., & Heckman, T. 2006, *MNRAS*, 372, 961, doi: [10.1111/j.1365-2966.2006.10859.x](https://doi.org/10.1111/j.1365-2966.2006.10859.x)
- Kroupa, P. 2001, *MNRAS*, 322, 231, doi: [10.1046/j.1365-8711.2001.04022.x](https://doi.org/10.1046/j.1365-8711.2001.04022.x)
- Lacy, M., Petric, A. O., Sajina, A., et al. 2007, *AJ*, 133, 186, doi: [10.1086/509617](https://doi.org/10.1086/509617)
- Lacy, M., Storrie-Lombardi, L. J., Sajina, A., et al. 2004, *ApJS*, 154, 166, doi: [10.1086/422816](https://doi.org/10.1086/422816)
- Lacy, M., Ridgway, S. E., Gates, E. L., et al. 2013, *ApJS*, 208, 24, doi: [10.1088/0067-0049/208/2/24](https://doi.org/10.1088/0067-0049/208/2/24)
- Lawrence, A., Warren, S. J., Almaini, O., et al. 2007, *MNRAS*, 379, 1599, doi: [10.1111/j.1365-2966.2007.12040.x](https://doi.org/10.1111/j.1365-2966.2007.12040.x)
- Lee, J. C., Hwang, H. S., & Ko, J. 2013, *ApJ*, 774, 62, doi: [10.1088/0004-637X/774/1/62](https://doi.org/10.1088/0004-637X/774/1/62)
- Levenson, N. A., Krolik, J. H., Życki, P. T., et al. 2002, *ApJL*, 573, L81, doi: [10.1086/342092](https://doi.org/10.1086/342092)
- Lonsdale, C. J., Smith, H. E., Rowan-Robinson, M., et al. 2003, *PASP*, 115, 897, doi: [10.1086/376850](https://doi.org/10.1086/376850)
- Luo, B., Brandt, W. N., Xue, Y. Q., et al. 2017, *ApJS*, 228, 2, doi: [10.3847/1538-4365/228/1/2](https://doi.org/10.3847/1538-4365/228/1/2)
- Lutz, D., Sturm, E., Tacconi, L. J., et al. 2008, *ApJ*, 684, 853, doi: [10.1086/590367](https://doi.org/10.1086/590367)
- Lyu, J., Alberts, S., Rieke, G. H., & Rujopakarn, W. 2022, arXiv e-prints, arXiv:2209.06219. <https://arxiv.org/abs/2209.06219>
- Marconi, A., & Hunt, L. K. 2003, *ApJL*, 589, L21, doi: [10.1086/375804](https://doi.org/10.1086/375804)
- McConnell, N. J., & Ma, C.-P. 2013, *ApJ*, 764, 184, doi: [10.1088/0004-637X/764/2/184](https://doi.org/10.1088/0004-637X/764/2/184)
- Mignoli, M., Vignali, C., Gilli, R., et al. 2013, *A&A*, 556, A29, doi: [10.1051/0004-6361/201220846](https://doi.org/10.1051/0004-6361/201220846)
- Mullaney, J. R., Alexander, D. M., Goulding, A. D., & Hickox, R. C. 2011, *MNRAS*, 414, 1082, doi: [10.1111/j.1365-2966.2011.18448.x](https://doi.org/10.1111/j.1365-2966.2011.18448.x)
- Nandra, K., Laird, E. S., Adelberger, K., et al. 2005, *MNRAS*, 356, 568, doi: [10.1111/j.1365-2966.2004.08475.x](https://doi.org/10.1111/j.1365-2966.2004.08475.x)
- Nandra, K., Laird, E. S., Aird, J. A., et al. 2015, *ApJS*, 220, 10, doi: [10.1088/0067-0049/220/1/10](https://doi.org/10.1088/0067-0049/220/1/10)
- Netzer, H. 2009, *MNRAS*, 399, 1907, doi: [10.1111/j.1365-2966.2009.15434.x](https://doi.org/10.1111/j.1365-2966.2009.15434.x)
- Ogawa, S., Ueda, Y., Tanimoto, A., & Yamada, S. 2021, *ApJ*, 906, 84, doi: [10.3847/1538-4357/abcce](https://doi.org/10.3847/1538-4357/abcce)
- Oliver, S. J., Bock, J., Altieri, B., et al. 2012, *MNRAS*, 424, 1614, doi: [10.1111/j.1365-2966.2012.20912.x](https://doi.org/10.1111/j.1365-2966.2012.20912.x)
- Padovani, P., Alexander, D. M., Assef, R. J., et al. 2017, *A&A Rv*, 25, 2, doi: [10.1007/s00159-017-0102-9](https://doi.org/10.1007/s00159-017-0102-9)
- Page, M. J., Symeonidis, M., Vieira, J. D., et al. 2012, *Nature*, 485, 213, doi: [10.1038/nature11096](https://doi.org/10.1038/nature11096)
- Reyes, R., Zakamska, N. L., Strauss, M. A., et al. 2008, *AJ*, 136, 2373, doi: [10.1088/0004-6256/136/6/2373](https://doi.org/10.1088/0004-6256/136/6/2373)
- Rieke, G. H., Alonso-Herrero, A., Weiner, B. J., et al. 2009, *ApJ*, 692, 556, doi: [10.1088/0004-637X/692/1/556](https://doi.org/10.1088/0004-637X/692/1/556)
- Rosario, D. J., Santini, P., Lutz, D., et al. 2012, *A&A*, 545, A45, doi: [10.1051/0004-6361/201219258](https://doi.org/10.1051/0004-6361/201219258)
- Roseboom, I. G., Oliver, S. J., Kunz, M., et al. 2010, *MNRAS*, 409, 48, doi: [10.1111/j.1365-2966.2010.17634.x](https://doi.org/10.1111/j.1365-2966.2010.17634.x)
- Runnoe, J. C., Brotherton, M. S., & Shang, Z. 2012, *MNRAS*, 426, 2677, doi: [10.1111/j.1365-2966.2012.21644.x](https://doi.org/10.1111/j.1365-2966.2012.21644.x)
- Santini, P., Rosario, D. J., Shao, L., et al. 2012, *A&A*, 540, A109, doi: [10.1051/0004-6361/201118266](https://doi.org/10.1051/0004-6361/201118266)
- Schreiber, C., Pannella, M., Elbaz, D., et al. 2015, *A&A*, 575, A74, doi: [10.1051/0004-6361/201425017](https://doi.org/10.1051/0004-6361/201425017)
- Shao, L., Lutz, D., Nordon, R., et al. 2010, *A&A*, 518, L26, doi: [10.1051/0004-6361/201014606](https://doi.org/10.1051/0004-6361/201014606)
- Shimizu, T. T., Mushotzky, R. F., Meléndez, M., et al. 2017, *MNRAS*, 466, 3161, doi: [10.1093/mnras/stw3268](https://doi.org/10.1093/mnras/stw3268)
- Shin, J., Woo, J.-H., Chung, A., et al. 2019, *ApJ*, 881, 147, doi: [10.3847/1538-4357/ab2e72](https://doi.org/10.3847/1538-4357/ab2e72)
- Somerville, R. S., Hopkins, P. F., Cox, T. J., Robertson, B. E., & Hernquist, L. 2008, *MNRAS*, 391, 481, doi: [10.1111/j.1365-2966.2008.13805.x](https://doi.org/10.1111/j.1365-2966.2008.13805.x)
- Springel, V., Di Matteo, T., & Hernquist, L. 2005, *MNRAS*, 361, 776, doi: [10.1111/j.1365-2966.2005.09238.x](https://doi.org/10.1111/j.1365-2966.2005.09238.x)
- Stalevski, M., Fritz, J., Baes, M., Nakos, T., & Popović, L. Č. 2012, *MNRAS*, 420, 2756, doi: [10.1111/j.1365-2966.2011.19775.x](https://doi.org/10.1111/j.1365-2966.2011.19775.x)
- Stalevski, M., Ricci, C., Ueda, Y., et al. 2016, *MNRAS*, 458, 2288, doi: [10.1093/mnras/stw444](https://doi.org/10.1093/mnras/stw444)
- Stanley, F., Harrison, C. M., Alexander, D. M., et al. 2015, *MNRAS*, 453, 591, doi: [10.1093/mnras/stv1678](https://doi.org/10.1093/mnras/stv1678)
- Stern, D., Eisenhardt, P., Gorjian, V., et al. 2005, *ApJ*, 631, 163, doi: [10.1086/432523](https://doi.org/10.1086/432523)
- Suzuki, T. L., Kodama, T., Sobral, D., et al. 2016, *MNRAS*, 462, 181, doi: [10.1093/mnras/stw1655](https://doi.org/10.1093/mnras/stw1655)
- Tremaine, S., Gebhardt, K., Bender, R., et al. 2002, *ApJ*, 574, 740, doi: [10.1086/341002](https://doi.org/10.1086/341002)
- Vanden Berk, D. E., Richards, G. T., Bauer, A., et al. 2001, *AJ*, 122, 549, doi: [10.1086/321167](https://doi.org/10.1086/321167)
- Vignali, C., Mignoli, M., Gilli, R., et al. 2014, *A&A*, 571, A34, doi: [10.1051/0004-6361/201424791](https://doi.org/10.1051/0004-6361/201424791)
- Volonteri, M., Capelo, P. R., Netzer, H., et al. 2015, *MNRAS*, 449, 1470, doi: [10.1093/mnras/stv387](https://doi.org/10.1093/mnras/stv387)
- Wilkes, B. J., Kilgard, R., Kim, D.-W., et al. 2009, *ApJS*, 185, 433, doi: [10.1088/0067-0049/185/2/433](https://doi.org/10.1088/0067-0049/185/2/433)

- Xie, Y., Ho, L. C., Zhuang, M.-Y., & Shanguan, J. 2021, ApJ, 910, 124, doi: [10.3847/1538-4357/abe404](https://doi.org/10.3847/1538-4357/abe404)
- Yan, R., Ho, L. C., Newman, J. A., et al. 2011, ApJ, 728, 38, doi: [10.1088/0004-637X/728/1/38](https://doi.org/10.1088/0004-637X/728/1/38)
- Yan, W., Hickox, R. C., Chen, C.-T. J., et al. 2021, ApJ, 914, 83, doi: [10.3847/1538-4357/abfaa0](https://doi.org/10.3847/1538-4357/abfaa0)
- Yang, G., Boquien, M., Buat, V., et al. 2020, MNRAS, 491, 740, doi: [10.1093/mnras/stz3001](https://doi.org/10.1093/mnras/stz3001)
- Zakamska, N. L., Strauss, M. A., Krolik, J. H., et al. 2003, AJ, 126, 2125, doi: [10.1086/378610](https://doi.org/10.1086/378610)
- Zhang, K., & Hao, L. 2018, ApJ, 856, 171, doi: [10.3847/1538-4357/aab207](https://doi.org/10.3847/1538-4357/aab207)